J. Wind Eng. Ind. Aerodyn. 132 (2014) 27–36

Contents lists available at ScienceDirect

Journal of Wind Engineering and Industrial Aerodynamics

journal homepage: www.elsevier.com/locate/jweia

An experimental study on the unsteady vortices and turbulent flow structures around twin-box-girder bridge deck models with different gap ratios

Wen-Li Chen [a,b,c], Hui Li [a,b,*], Hui Hu [c]

[a] Key Lab of Structures Dynamic Behavior and Control, Harbin Institute of Technology, Ministry of Education, Harbin, Heilongjiang 150090, China
[b] School of Civil Engineering, Harbin Institute of Technology, Harbin, Heilongjiang 150090, China
[c] Department of Aerospace Engineering, Iowa State University, Ames, IA 50011, USA

ARTICLE INFO

Article history:
Received 1 January 2014
Received in revised form
4 June 2014
Accepted 7 June 2014
Available online 5 July 2014

Keywords:
Twin-box-girder
Bridge deck model
Gap ratio
Unsteady vortex
Flow structure
PIV
Pressure

ABSTRACT

In the present study, an experimental investigation was conducted to characterize the unsteady vortices and turbulent flow structures around twin-box-girder (TBG) bridge deck models with and without cross beams. While the oncoming wind speed was fixed at $U_\infty = 8.0$ m/s (i.e., the corresponding Reynolds number, $Re = 1.01 \times 10^4$, based on the height of the box girder) during the experiments, the gap width between the TBG was varied to have four different gap ratios (i.e., the ratio of the gap width between the TBG to the deck height). The corresponding test cases were classified into two categories: the cases with relatively small gap ratios (i.e., gap ratio = 0.85 and 1.70) and the cases with relatively large gap ratios (i.e., gap ratio = 2.55 and 3.40). In addition to measuring the surface pressure distributions around the TBG bridge deck models using an array of digital pressure transducers, a high-resolution particle image velocimetry (PIV) system was utilized to perform detailed flow field measurements to quantify the evolution of the unsteady vortex structures around the TBG bridge deck models. The measurements reveal that as the gap ratio increases, the vortex shedding moves from the trailing edge of the leeward box to the rear edge of the windward box, which simultaneously increases the turbulent kinetic energy in the gap region and the fluctuating pressures on the leeward box. The vortex dimensions and the core-to-core distances between two neighboring vortices are also affected by the gap ratio. Combining with the estimation of the pressure field and the measured fluctuating pressure coefficient distributions on the TBG models, it is found that the TBG bridges with larger gap ratios will dramatically strengthen the fluctuating pressure coefficients on the leeward box which are greatly higher than those for the small gap ratio cases. Moreover, for large gap ratio cases, the test model with cross beams also has higher fluctuating pressure coefficients on the leeward box which just decrease a little comparing with the test model without cross beams.

1. Introduction

As the bridge span increases, modern cable-stayed and suspension bridges are becoming more flexible and have little damping capability. While single box steel girders usually cannot meet the requirements of the aerodynamic stability for long-span bridges as the girder width increases, twin-separated box steel girders, which are composed of two parallel longitudinal girders with an open gap between them, are found to be able to improve the aerodynamic stability for long-span bridges. For twin-box-girders (TBG) bridges, the two parallel girders are usually connected by transverse cross beams. So far, several super-long-span bridges have been constructed by using the TBG section configuration, which include the Xihoumen suspension bridge (main span: 1650 m, China), the Gwangyang suspension bridge (main span: 1545 m, Korea), the Hong Kong Stonecutters cable-stayed bridge (main span: 1018 m, China) and Edong cable-stayed bridge (main span: 926 m, China). While the super-long-span bridges with TBG configuration have better flutter performance (i.e., higher critical flutter speed than those with single box girders (Ge and Xiang, 2008)), the flow characteristics around such kind of bridge decks are more complicated due to the effects of the gap between the two separated box girders.

While the TBG configuration is relatively new for long-span cable-supported bridges, in the past decade several investigations have been conducted on TBG bridges. Diana et al. (2004, 2006) conducted wind tunnel tests to investigate the aerodynamic forces (i.e., the static aerodynamic coefficients, flutter derivatives, admittance

* Corresponding author.
E-mail address: lihui@hit.edu.cn (H. Li).

http://dx.doi.org/10.1016/j.jweia.2014.06.015
0167-6105/

functions) of the multiple box deck of the Messina Strait Bridge and proposed a numerical model to reproduce the aerodynamic forces induced by the vortex shedding. Kwok et al. (2012) conducted wind-induced pressure measurements around a sectional twin-deck bridge model to study the effects of gap-width on the aerodynamic forces and vortex shedding mechanisms. They found that, for larger gap-width configurations, the downstream deck was supposed to be immersed in the wake of the upstream deck. Large mean positive pressures were recorded at the upstream windward surface of the downstream deck, which results in a significant increase of the drag force acting on the deck. They also found that the effect of the gap-width on the lift force and pitching moment is smaller than that of the angle of wind incidence on the lift force and pitching moment; however, both the gap-width and the angle of wind incidence have an evident effect on the drag force.

Ogawa et al. (2002) investigated the aerodynamic characteristics of a TBG section that could be adapted for a super-long span suspension bridge. They found that the steady pitching moment characteristics and flutter stability could be greatly improved by attaching rails on the bottom of the fairing and attaching vertical plates to the lower flange of the girder. Larsen et al. (2008) conducted an investigation on the vortex characteristics of a twin box bridge section at different Reynolds numbers. They found that the vortex shedding of TGBs became stronger than that of mono box girders because the fluctuating pressure on the downwind box was dramatically larger than that on the upwind box; specifically, the vortices shed from the upwind box would impinge onto the downwind box, resulting in higher fluctuating pressures than those on the upwind box where the vortices were shed. The analytical results indicated that the guide vanes were efficient devices for inducing high speed flow in the wake region of the upwind box to prevent vortex formation. It was also found that, the flutter critical wind speed can be dramatically increased for the TBG bridge deck, which was highly desirable for very long span cable supported bridges comparing with a mono box deck with the same span. However, the down side of TBG bridge decks was the vortex shedding which would cause higher fluctuating pressures on the downwind box (Larsen et al., 2008).

While these previous studies revealed are very useful, more work is still needed to improve our understanding of the underlying physics of the flow structures around complex multiple-box girders, especially the behavior of the unsteady vortex shedding and turbulent flow characteristics around multiple-box girders. In the present study, experiments were conducted to investigate the flow characteristics around fixed TBG models with different gap ratios. In addition to measuring the surface pressure distributions around the TBG bridge deck models using an array of digital pressure transducers, a high-resolution particle image velocimetry (PIV) system was utilized to perform detailed flow field measurements to quantify the evolution of the unsteady vortex structures around the TBG bridge deck models. The detailed flow field measurements were correlated with the measured pressure distributions around the test models to elucidate the underlying physics and to quantify the influence of the gap ratio on the evolutions of the unsteady vortices and turbulent flow structures around the test models. It should be noted that this study only focused on the flow characteristics and aerodynamic forces of the fixed TBG bridge deck models, which are different from the vortex-induced vibration, and the corresponding flow characteristics and aerodynamic forces under occurrence of vortex-induced vibration.

2. Experimental setup and test models

The experimental study was conducted in a closed-circuit low-speed wind tunnel located in the Aerospace Engineering Department of Iowa State University. The tunnel has a test section with a 1.0×1.0 ft^2 (30.48×30.48 cm^2) cross section, and the walls of the test section are optically transparent. The tunnel has a contraction section upstream of the test section with honeycombs, screen structures, and a cooling system installed to provide uniform, low-turbulence flow in the test section. The turbulence level of the oncoming flow at the entrance of the test section is about 0.8% as measured by a hotwire anemometer.

2.1. Test models

Fig. 1 shows the TBG test models used in the present study. The test models have a height of $H=18.240$ mm and width of $L=78.125$ mm for each box girder. The angle of attack of each box girder was set to zero. During the experiments, the total deck width was changed according to the different gap widths between the girders, and the corresponding gap ratio was varied from 0.85 to 3.40 (i.e., 0.85, 1.70, 2.55 and 3.40). It should be noted that the test model with the gap ratio of 1.70 for the present study is a scaled-down version of the model reported in Laima et al. (2013) (with a scale factor of 4.806) from where the detailed information of the test model is given. The speed of the oncoming airflow was fixed at $U_\infty=8.0$ m/s during the experiments, with a corresponding test model Reynolds number of $\mathrm{Re}=1.01 \times 10^4$ based on the height of the box girder and the oncoming wind speed.

Since the gap between the two box girders is shaded by the cross beams for the acquisition PIV images, the deck model #1 without cross beams (Fig. 1(a)) was used at first to measure the flow structures in the gap between the two girders. Then, the deck model #2 (Fig. 1(b)) with cross beams was used to investigate the effects of the gap width on the flow structures around the test model. The laser illumination plane for the PIV measurements was set at the same position for the test models with or without cross beams, specifically, at the middle plane of the 4th gap.

As shown in Fig. 2, a total amount of 62 pressure taps (i.e., 31 for each box) were arranged around the TBG models. The pressure taps were located in the same cross section as the PIV measurement plane. For each pressure tap, the pressure measurements

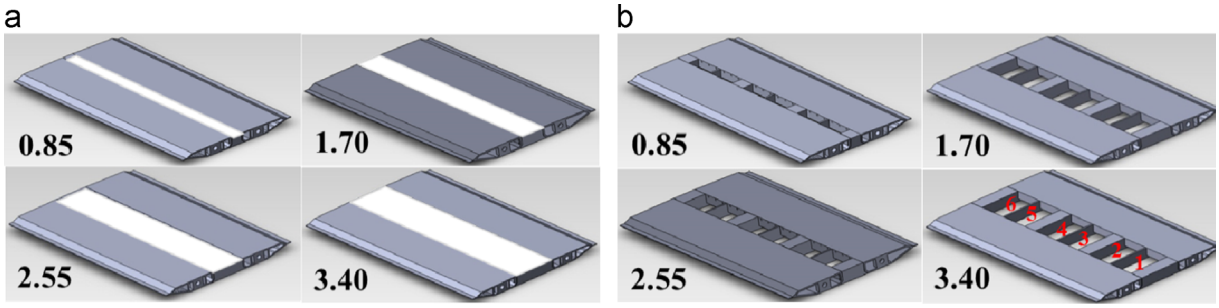

Fig. 1. Testing deck models with different gap ratios, (a) model #1, (b) model #2.

Fig. 2. Pressure tap distribution on the pressure measurement section (gap ratio = 1.70).

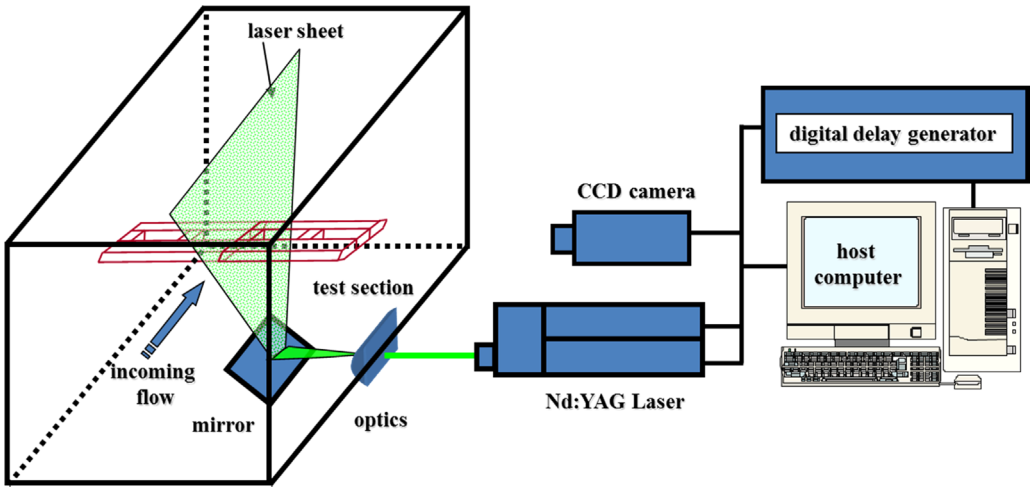

Fig. 3. Schematic of the experimental setup.

were conducted at a sampling rate of 300 Hz and with a total sampling time of 60 s. The blockage ratios for the test models were about 6.0%, and the measured pressures on the test model were corrected to account for the solid blockage and the wake blockage (Barlow et al., 1999). Based on the work of Irwin et al. (1979), the amplitude attenuation and phase lag of the pressure signals caused by the 0.4 m long tygon tubing used for the pressure measurements are expected to be quite small for the pressure signals at the frequencies lower than 300 Hz.

2.2. Experimental setup for PIV measurements

A high-resolution particle image velocity (PIV) system was employed to characterize the unsteady vortex shedding and turbulent flow structures around the TBG models. Fig. 3 shows the schematic of the experimental setup used for the PIV measurements. The oncoming airflow was seeded with 1–5 μm oil droplets. Illumination was provided by a double-pulsed Nd:YAG laser (New Wave Gemini PIV 120-15) adjusted on the second harmonic and emitting two pulses of 120 mJ at the wavelength of 532 nm with a repetition rate of 8 Hz. The laser beam was shaped to a sheet by a set of mirrors and a set of spherical and cylindrical lenses. The thickness of the laser sheet in the measurement region was about 1.0 mm. During the experiments, a mirror was installed on the top of the wind tunnel to reflect the illuminating laser sheet back to the measurement region to eliminate the shadow region of the test model for PIV measurements. A high-resolution 12-bit (1376 × 1040 pixels) CCD camera (SensiCam, CookeCorp) was employed to perform PIV image recording. The distance between the laser sheet and image recording plane of the CCD camera was about 1000 mm. The CCD camera and double-pulsed Nd:YAG lasers were connected to a workstation (host computer) via a digital delay generator (Berkeley Nucleonics, Model 565), which controlled the timing of the laser illumination and image acquisition.

Instantaneous PIV velocity vectors were obtained from the acquired PIV images by using a frame-to-frame cross-correlation technique involving successive patterns of particle images in a 32 × 32 pixels interrogation window. An effective overlap of 50% of the interrogation window size was employed in PIV image processing. After the instantaneous velocity vectors (U, V) were determined, instantaneous spanwise vorticity (ω_z) was derived. For each of the test cases, the distributions of the ensemble-averaged flow quantities such as mean velocity ($\overline{U}$, $\overline{V}$), ensemble-averaged spanwise vorticity (Ω_z), turbulent velocity fluctuations (u, v) and normalized turbulent kinetic energy distributions (i.e., T.K.E. $= (u^2+v^2)/(2U_\infty^2)$) were obtained from a cinema sequence of about 500 instantaneous velocity fields. For the PIV measurement results given in the present study, the measurement uncertainty of the velocity vectors is estimated to be within 1.0% and the measurement uncertainty of the turbulent velocity fluctuations (u, v) and T.K.E. are about 5.0%.

3. Experimental results and discussions

3.1. Determination of swirling strength to visualize vortex structures

As we all know, vorticity analysis is often performed to identify vortex location and to study vortex characteristics, i.e., size, strength, rotation direction, etc. Vorticity, ω, is defined as

$$\omega = \nabla \times \mathbf{u} \tag{1}$$

where $\mathbf{u}$ is the velocity vector (u, v) of the flow field and ∇ is the Hamilton operator. For a two-dimensional incompressible flow, the vorticity in the z direction can be written as

$$\omega_z = \frac{\partial v}{\partial x} - \frac{\partial u}{\partial y} \tag{2}$$

where x and y are the coordinates along the in-flow and cross flow directions, respectively. According to Eq. (2), the vorticity can not only identify vortex motion but also any shearing motion present in the flow. In wall turbulence, the strong shear layers existing in the near-wall region will conceal the virtual turbulence eddies, and the shearing motions will make reliable calculation of the virtual vortices difficult as shown in Fig. 4(a). Fig. 4(a) shows that whole shear layer is computed as the vortices. The vortex forming,

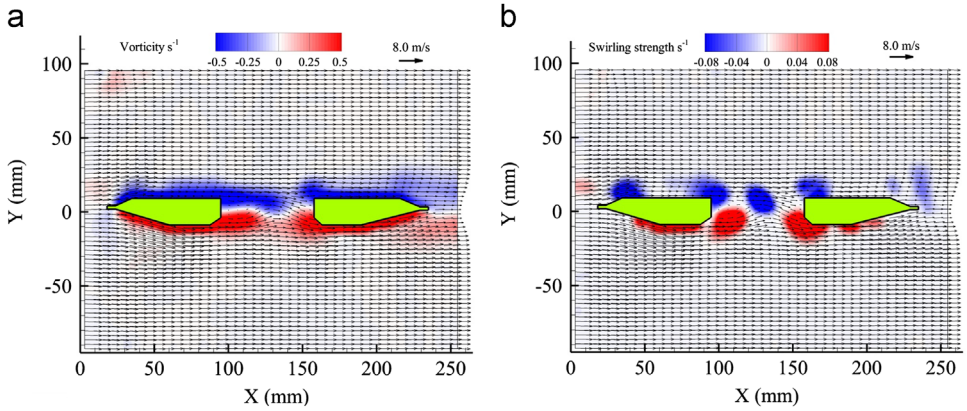

Fig. 4. Flow structure around the TBG model, (a) vorticity and (b) swirling strength.

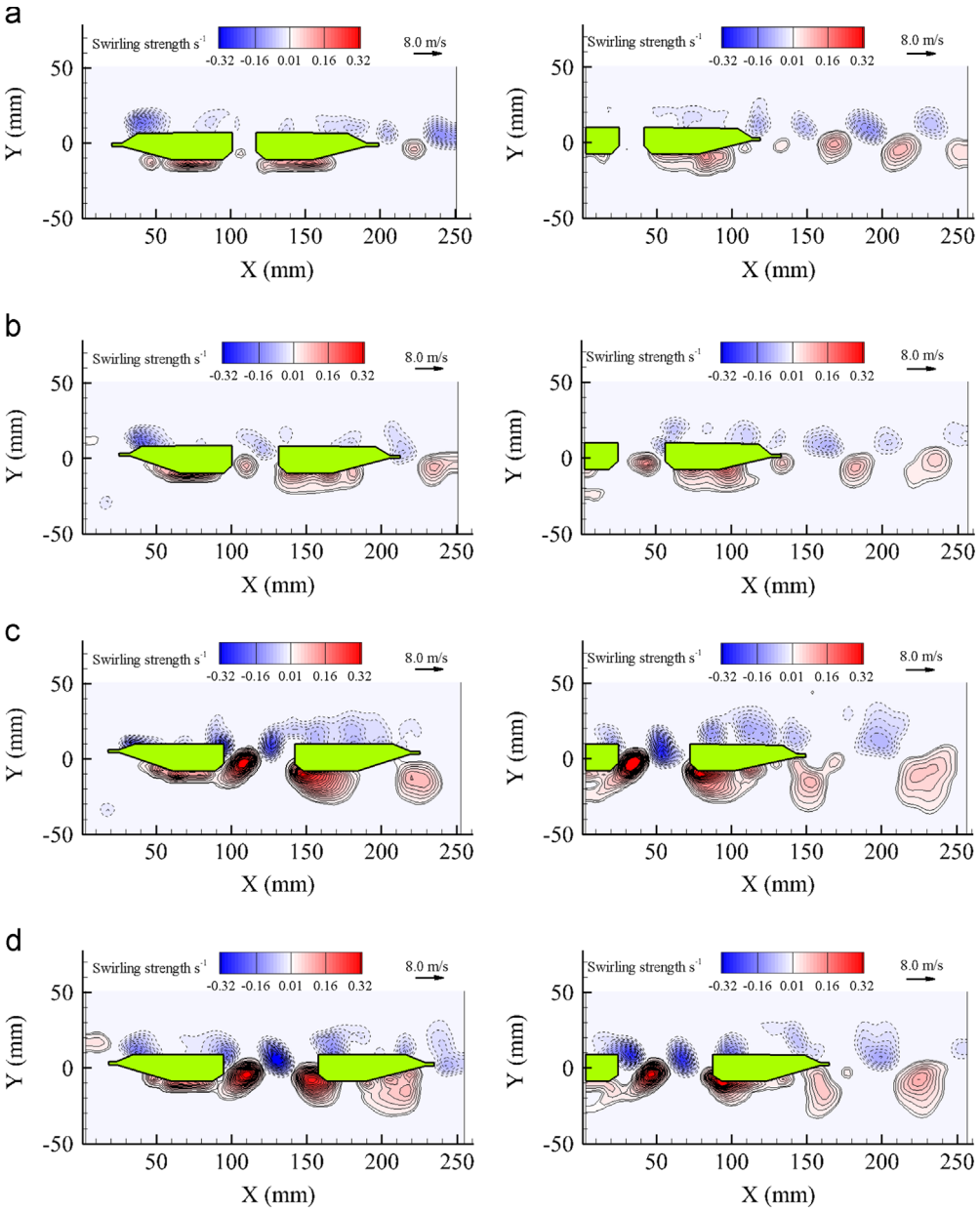

Fig. 5. Instantaneous vorticity distributions around the test model #1, (a) gap ratio=0.85, (b) gap ratio=1.70, (c) gap ratio=2.55, and (d) gap ratio=3.40.

shedding locations and statistics cannot be clearly identified. To overcome this shortcoming, we prefer to use the imaginary part of the complex eigenvalue of the velocity gradient tensor to distinctly visualize vortices (Zhou et al., 1999). Since the two-dimensional flow velocity fields are obtained through the PIV measurements, the full velocity gradient tensor cannot be formed and we can only set up a two-dimensional form of the velocity gradient tensor as

$$D_{2-D} = \begin{bmatrix} \frac{\partial u}{\partial x} & \frac{\partial u}{\partial y} \\ \frac{\partial v}{\partial x} & \frac{\partial v}{\partial y} \end{bmatrix} \tag{3}$$

The determinant, D_{2-D}, should either have two real eigenvalues or a conjugate pair of complex eigenvalues, i.e., $\lambda_{cr} \pm \lambda_{ci} i$, where λ_{cr} and λ_{ci} are the real and the imaginary parts, respectively. As reported in Zhou et al. (1999), the strength of any local swirling motion is quantified by λ_{ci}, which is defined as the swirling strength of the vortex. Swirling strength is closely related to vorticity, but it can discriminate between vorticity due to shear motion and vorticity resulting from rotation as shown in Fig. 4(b). According to the results shown in Fig. 4(a) and (b), only the swirling strength results of the flow structures around TBG models will be given in the following analysis.

3.2. Flow structures around TBG models with different gap ratios

Vortex shedding and flow structures around twin-box girder models with four gap ratios ranging from 0.85 to 3.40 were studied. Fig. 5 shows the instantaneous swirling strength at different gap ratios based on the 2-D PIV measurements. For each gap ratio case, two subfigures are listed: the left subfigures show the instantaneous swirling strength distributions around the test model; and the right subfigures show the instantaneous swirling strength distributions located in the wake of the test model. The PIV measurement results indicate clearly that unsteady vortices mainly shed from the trailing edges of the leeward box when the gap ratio is relatively small (i.e., for the cases with gap ratio being 0.85 and 1.70). As the gap ratio increases (i.e., for the cases with gap ratio being 2.55 and 3.40), flow separation occurs at upstream locations and unsteady vortices shed from the rear edges of the windward box and impinge on the leeward box. As reported by Larsen et al. (2008), the vortices that shed from the windward box and impinge on the leeward box result in higher fluctuating pressures on the leeward box than on the windward. The corresponding fluctuating pressures on the test models will be quantitatively discussed in the later section of the present study.

As shown in Fig. 6, the time-averaged T.K.E. distributions indicate that the T.K.E. level in the gap region and the down side of twin box bridge decks increases with increasing the gap ratio; hence, the vortex shedding is gradually enhanced, which results in larger velocity fluctuations in the gap region.

Fig. 7 shows the instantaneous swirling strength and time-average T.K.E. distributions at the gap ratio of 3.40 for test model #2. Compared with the results shown in Figs. 5(d) and 6(d), there is no visible difference for the flow structures around two test models. The smaller variations in two test models will be analyzed through the pressure distributions in the later section.

The core-to-core distance of two neighboring vortices in the horizontal and vertical directions was analyzed to further explain the effect of the gap ratio on the vortices and flow structures. Fig. 8(a) shows clearly the horizontal core-to-core distance of two neighboring vortices in the gap region at three different gap ratios (omitting the case of the gap ratio of 0.85 where there is no distinct vortex shedding in the gap region). The mean values and root mean squares (RMS) of the horizontal core-to-core distances of two neighboring vortices are 10.98 ± 3.29, 17.74 ± 3.25 and 19.60 ± 2.70 mm for these three cases (i.e., gap ratio=1.70, 2.55 and 3.40). The corresponding gap widths of these three cases are 31.01, 46.51 and 62.02 mm, respectively. For the larger gap ratio cases (i.e., gap ratio=2.55 and 3.40), the horizontal core-to-core distances of two neighboring vortices were close and the gap width likely had little influence. For the case of gap ratio=1.70, the horizontal core-to-core distance of two neighboring vortices was greatly compressed to about half the distance seen in the larger gap ratio cases (i.e., gap ratio=2.55 and 3.40). Before the next vortex sheds from the trailing edge of the windward box, the previously shedding vortex has already impinged on the leading

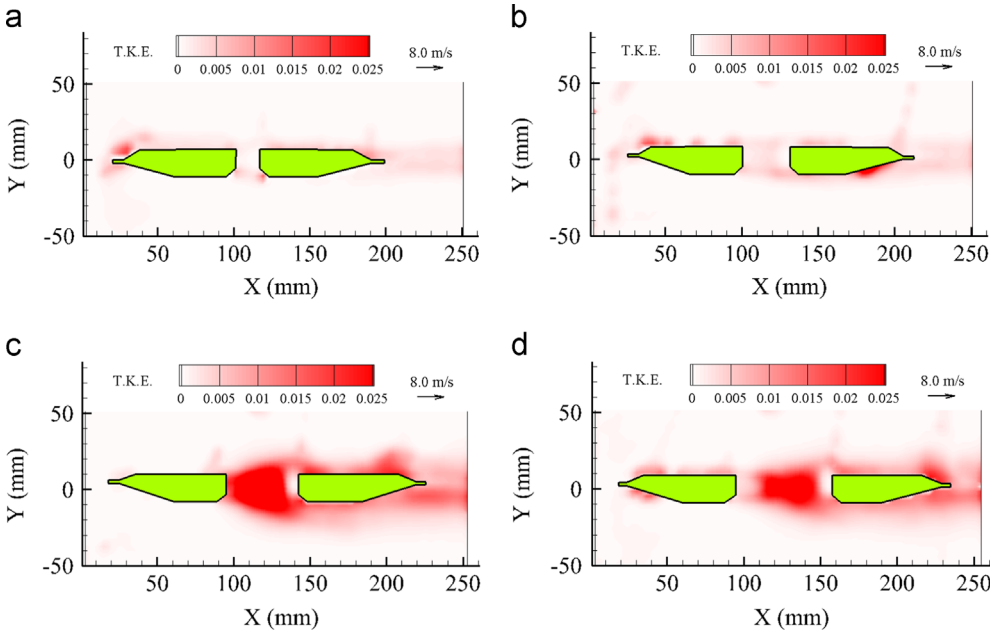

Fig. 6. Time-average T.K.E. distributions around the test model #1, (a) gap ratio=0.85, (b) gap ratio=1.70, (c) gap ratio=2.55, and (d) gap ratio=3.40.

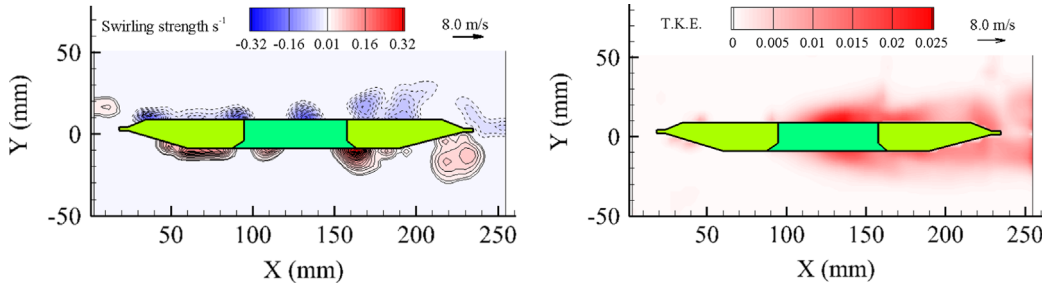

Fig. 7. Instantaneous vorticity (left) and time-average T.K.E. distributions (right) at gap ratio=3.40 for the test model #2.

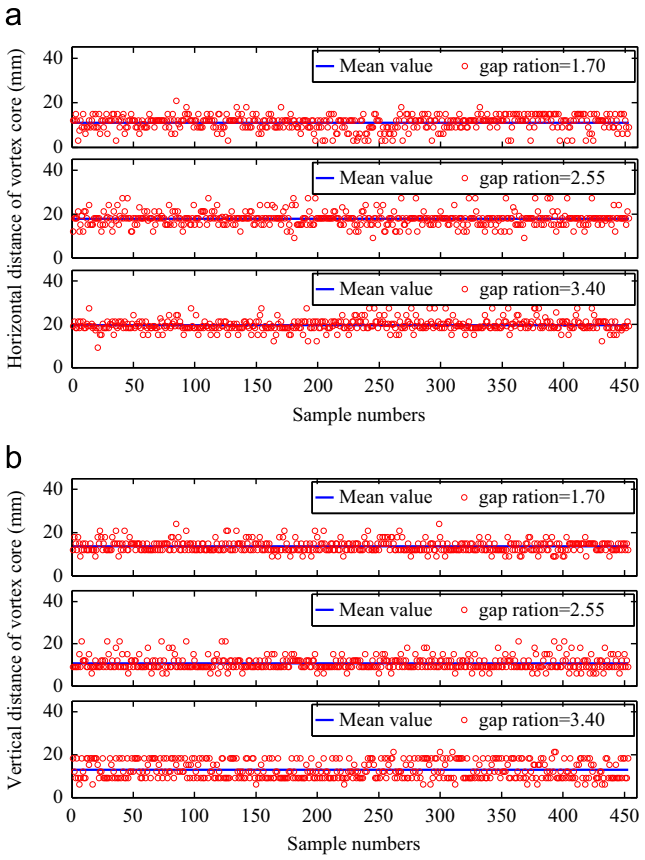

Fig. 8. Core-to-core distances of neighboring vortices for the test model #1, (a) horizontal distance and (b) vertical distance.

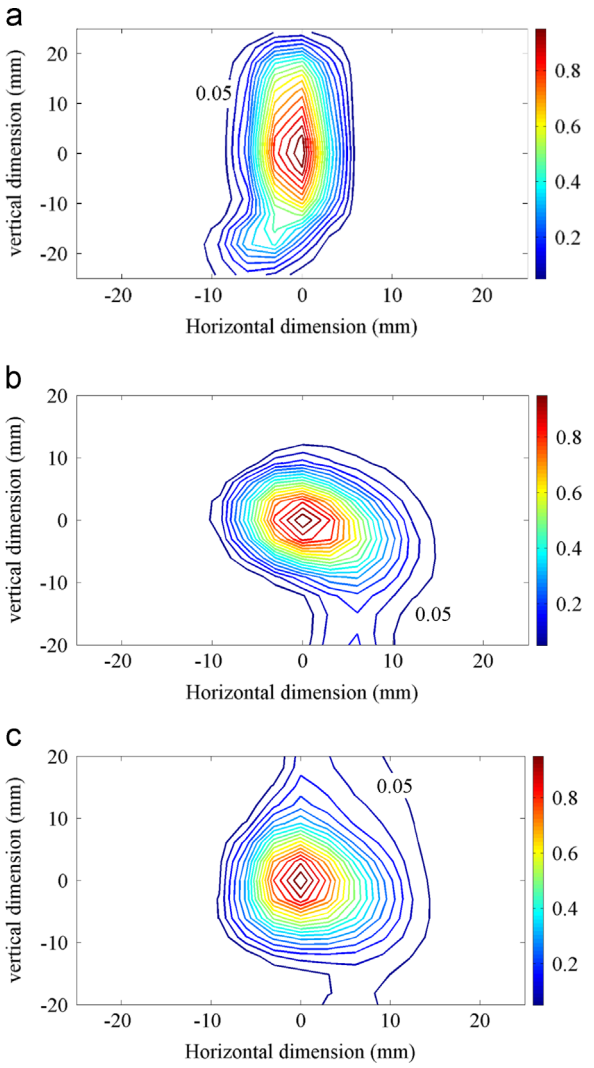

Fig. 9. Mean scales of the vortices for the test model #1, (a) gap ratio=1.70, (b) gap ratio=2.55, and (c) gap ratio=3.40.

edge of the leeward box. The impinging vortex is blocked and, therefore, it will compress the next vortex from the trailing edge of the windward box. As a result of this interaction, the normal propagation of the vortices is influenced by the narrower gap width.

As shown in Fig. 8(b), the mean values and RMS values of the vertical core-to-core distances of two neighboring vortices in the gap region at three different gap ratios (i.e., gap ratio=1.70, 2.55 and 3.40) are 13.61 ± 2.59, 10.71 ± 3.01 and 12.87 ± 4.06 mm, respectively. The gap width has a smaller effect on the vertical core-to-core distances of two neighboring vortices; however, for the case of gap ratio=1.70, the vortices are compressed in the horizontal direction and pulled a little in the vertical direction. The RMS values show the magnitude of the distance in the vertical direction that the vortices alternate. If the RMS values of the vertical core-to-core distances of two neighboring vortices equal zero, then the vortices shedding from upper and lower surfaces are parallel and are not alternating in the vertical direction. As the gap ratio increases, the RMS value of the vertical core-to-core distances of two neighboring vortices increases and the vortices alternate more intensely.

To measure the mean vortex shape from the instantaneous results shown in Fig. 5, the vortex with maximum swirling strength from each instantaneous measurement was statistically analyzed with all instantaneous vortex cores aligned to the same position (i.e., the coordinate origin (0,0)). The normalized mean swirling strength from 453 instantaneous results was then obtained as shown in Fig. 9. The horizontal dimensions of the

mean vortex shapes at different gap ratios (1.70, 255 and 3.40) are 14.15, 24.13 and 23.65 mm, respectively. For a small gap ratio=1.70, the gap width of 31.01 mm is not sufficient to accommodate two vortices if the horizontal dimensions are about 24 mm; therefore, the horizontal vortex dimension is compressed to 14.15 mm as a result of two vortices occupying a narrow gap width. For larger gap ratios (i.e., gap ratio=2.55 and 3.40), the gap widths are 46.51 and 62.02 mm. The vortices located in the gap region do not simultaneously reach the maximum swirling strength and the biggest size; hence, the gap can accommodate two or more vortices as shown in Fig. 5.

3.3. Estimation of pressure field around TBG models

The velocity variation may induce a pressure change in the flow field according to the Navier–Stokes equations. Based on the Navier–Stokes momentum equation, the pressure gradient can be written as

$$\nabla p = \rho\left(\nu\nabla^2\mathbf{u} - \frac{D\mathbf{u}}{Dt}\right) \tag{4}$$

where p is the pressure, ρ is the flow density, t is the time, and ν is the kinematic viscosity ($\nu=\mu/\rho$ with μ denoting the dynamic viscosity). While, two-dimensional PIV measurements are unable to obtain out-of-plane components (i.e., $\partial u/\partial z$, $\partial v/\partial z$, $\partial u^2/\partial z^2$ and $\partial v^2/\partial z^2$, z is the coordinate along the spanwise directions), it should be noted that the main flow was along the in-flow direction (i.e., x direction) and the vortex shedding alternated in the cross flow direction (i.e., y direction); therefore, the out-of-plane components were relatively small compared with the in-plane components. Additionally, the repetition rate of the PIV measurement in this test was just 8 Hz, which is low with respect to a vortex shedding frequency of about 100 Hz (i.e., the vortex shedding frequency of 96.67 Hz for the gap ratio=2.55 measured by a DSA pressure measurement system). The temporal parts (i.e., $\partial u/\partial t$ and $\partial v/\partial t$) and out-of-plane parts in Eq. (4) have to be neglected in the estimation process. We know this assumption will take some errors to pressure field estimation, but the main purpose of the pressure field estimation here is to find the difference of the pressure fluctuations of the flow field around the TBG models with different gap ratios. The simplified form of Eq. (4) can be expressed as

$$\frac{\partial p}{\partial x} = \mu\left(\frac{\partial^2 u}{\partial x^2} + \frac{\partial^2 u}{\partial y^2}\right) - \rho\left(u\frac{\partial u}{\partial x} + v\frac{\partial u}{\partial y}\right)$$
$$\frac{\partial p}{\partial y} = \mu\left(\frac{\partial^2 v}{\partial x^2} + \frac{\partial^2 v}{\partial y^2}\right) - \rho\left(u\frac{\partial v}{\partial x} + v\frac{\partial v}{\partial y}\right) \tag{5}$$

According to Eq. (5), we can estimate the pressure field around the test model #1 with different gap ratios. Fig. 10 shows the estimated fluctuating pressure coefficient field around the test model #1 with different gap ratios. Comparing the results between Figs. 5 and 10 shows that the vortex shedding occurs predominately in the wake of the leeward box and the relatively high level of T.K.E. is concentrated in the near wake of the model when the gap ratio is relatively smaller (i.e., gap ratio=0.85 and 1.70). Simultaneously, higher pressure fluctuations also located in this near wake region of the leeward box as shown in Fig. 10(a) and (b). As the gap ratio increases to 2.55 and 3.40, the vortices shed from upstream positions and impinge onto the leeward box, which increases the pressure fluctuating level in the region near to the wall of the leeward box as shown in Fig. 10(c) and (d). As a result, the pressure fluctuations on the leeward box should be much larger than those on the windward box for a TBG model with larger gap ratios (i.e., gap ratio=2.55 and 3.40). Comparing Fig. 10(a) and (b) with Fig. 10 (c) and (d), it is found that the pressure fluctuations near to the wall of the leeward box of the test model #1 with large gap ratios are higher than those with small gap ratios.

3.4. Wall pressure distributions on TBG models

For a quantitative analysis of the pressure distribution on the test models, the pressure measurement was simultaneously performed by a DSA pressure measurement system (the precision is 0.05% full scale of 2540 Pa). The pressure section as shown in Fig. 2 is co-located with the PIV measurement. The pressure distributions on test models #1 and #2 were employed to validate the characteristics of

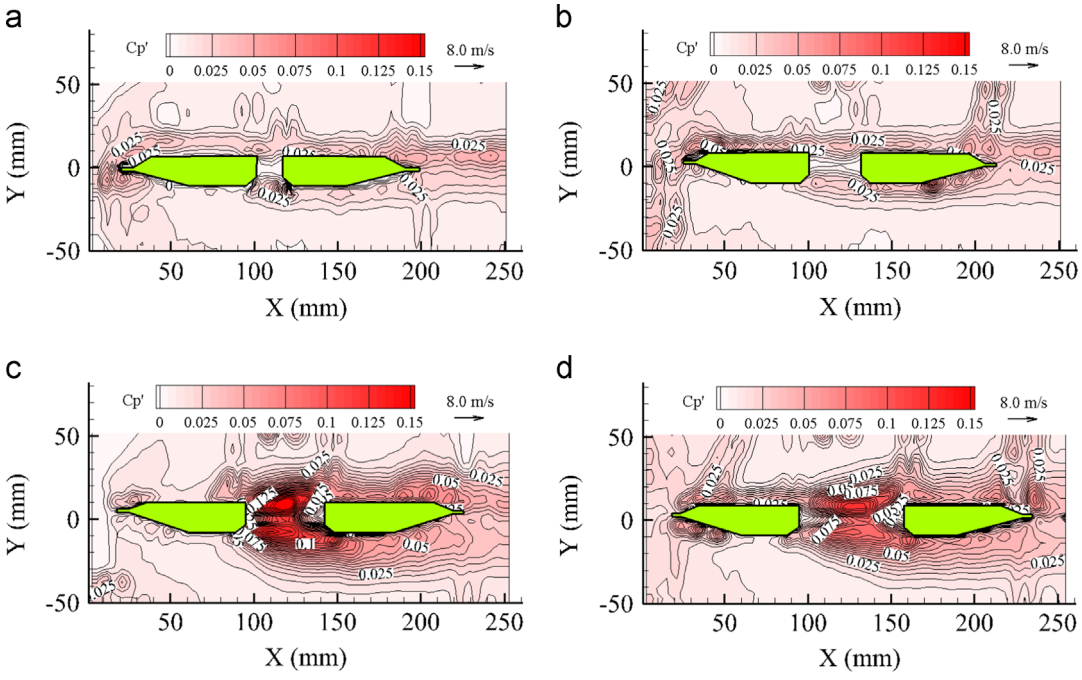

Fig. 10. Pressure fluctuation coefficients of flow field around test models with different gap ratios for the test model #1, (a) gap ratio=0.85, (b) gap ratio=1.70, (c) gap ratio=2.55, and (d) gap ratio=3.40.

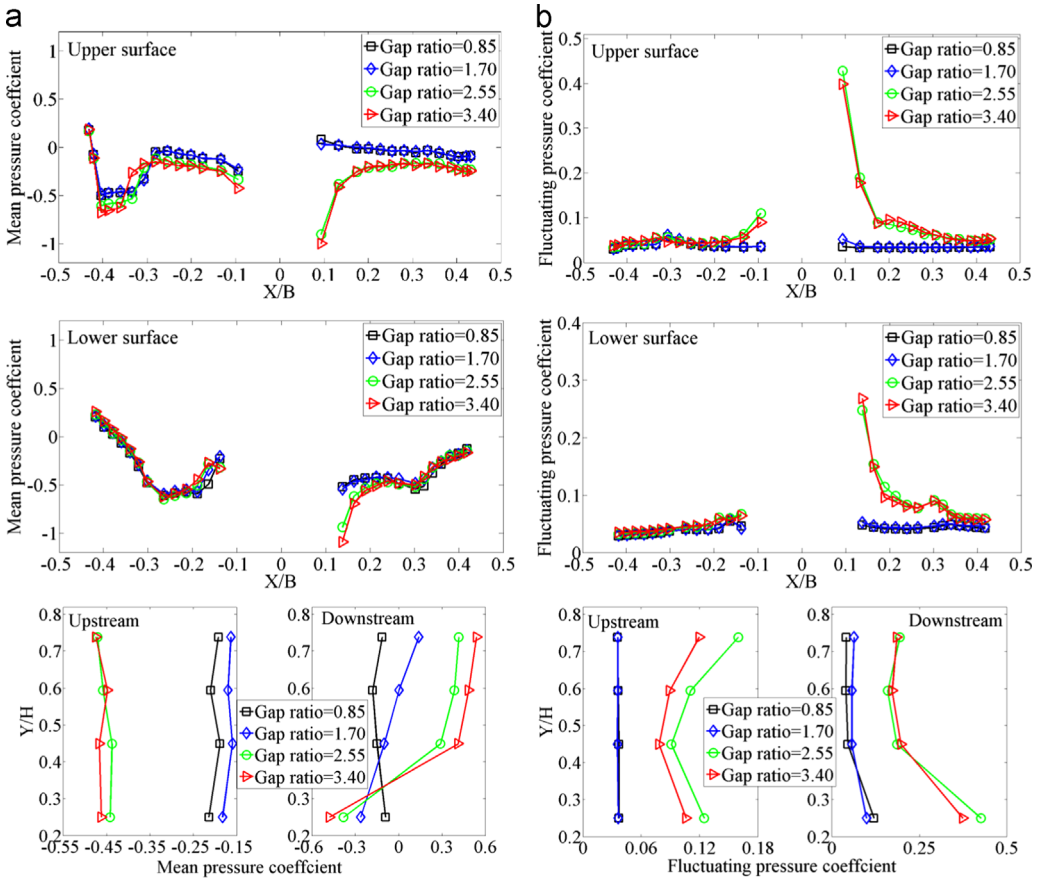

Fig. 11. Measured aerodynamic coefficients for the test model #1 with different gap ratios, (a) mean pressure coefficient and (b) fluctuating pressure coefficient.

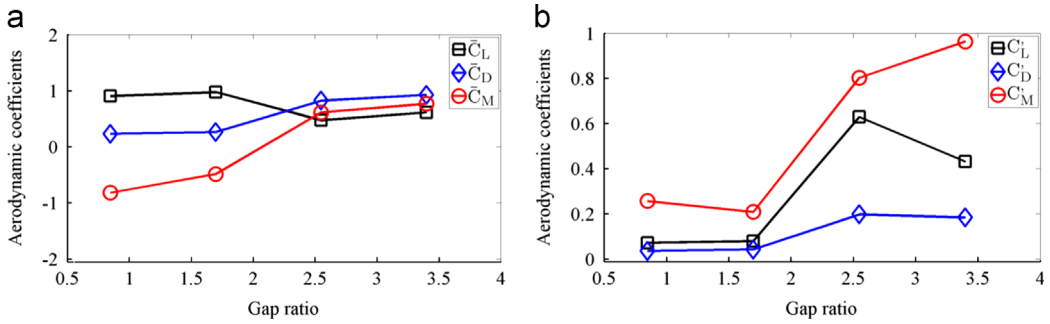

Fig. 12. Aerodynamic coefficients for the test model #1 with different gap ratios, (a) mean aerodynamic coefficients and (b) fluctuating aerodynamic coefficients.

the flow structures around the models. Fig. 11 shows the distributions of the mean and fluctuating pressure coefficients on the pressure section of the test model #1 for four gap ratios. For convenient comparisons of the aerodynamic force coefficients between these four cases, the gap ratio = 1.70 was used as reference in the figure-making process. As clearly shown in Fig. 11(a), the mean pressure coefficients on the windward are close for all the gap ratios. However, in the front regions of the leeward box, the positive pressure gradient changes into inverse negative gradient on the upper surface and the negative pressure gradient on the lower surface strengthens when the gap ratio increases. This suggests that flow separation may occur from the leading edge of the upper surface and be enhanced on the front part on the lower surface.

Combining the results of the swirling strength by the PIV measurements and the measured fluctuating pressure distribution (RMS values) on the test model #1 as shown in Fig. 11(b), it is found that the vortices shed from the trailing edges of the windward box and impinge onto the leading edges of leeward box at large gap ratios. The vortex shedding from the trailing edges of the windward box increases the local fluctuating pressure coefficients. The vortices moving across the gap region enhance

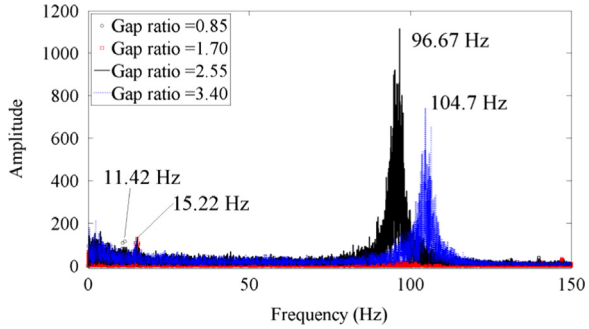

Fig. 13. Frequency spectra of lift coefficients of the test models with different gap ratios.

the fluctuating pressure coefficients on both sides of the gap region. Additionally, the vortex impinging on the leeward box dramatically increases the fluctuating pressure coefficients on the front edges of the leeward box at large gap ratios. Together, the measured pressure coefficient distributions and the measured flow structures on the TBG models show a consistent relationship between the fluctuating pressures and unsteady flow structures.

The aerodynamic forces (i.e., lift, drag, and moment) are calculated by integrating the surface pressure of the twin separated box girders. As the girder width changes with the gap ratio, the lift, drag and moment force coefficients per length are defined as

$$C_L = \frac{F_L}{\frac{1}{2}\rho U_\infty H},\ C_D = \frac{F_D}{\frac{1}{2}\rho U_\infty H},\ C_M = \frac{M}{\frac{1}{2}\rho U_\infty H^2} \tag{6}$$

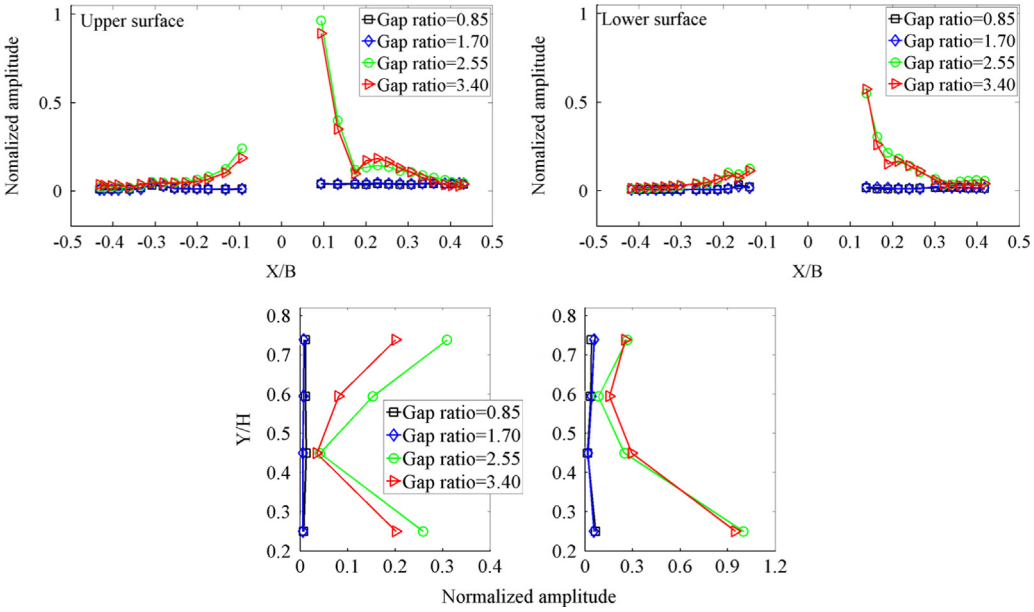

Fig. 14. Aerodynamic coefficients for the test model #1 with different gap ratios.

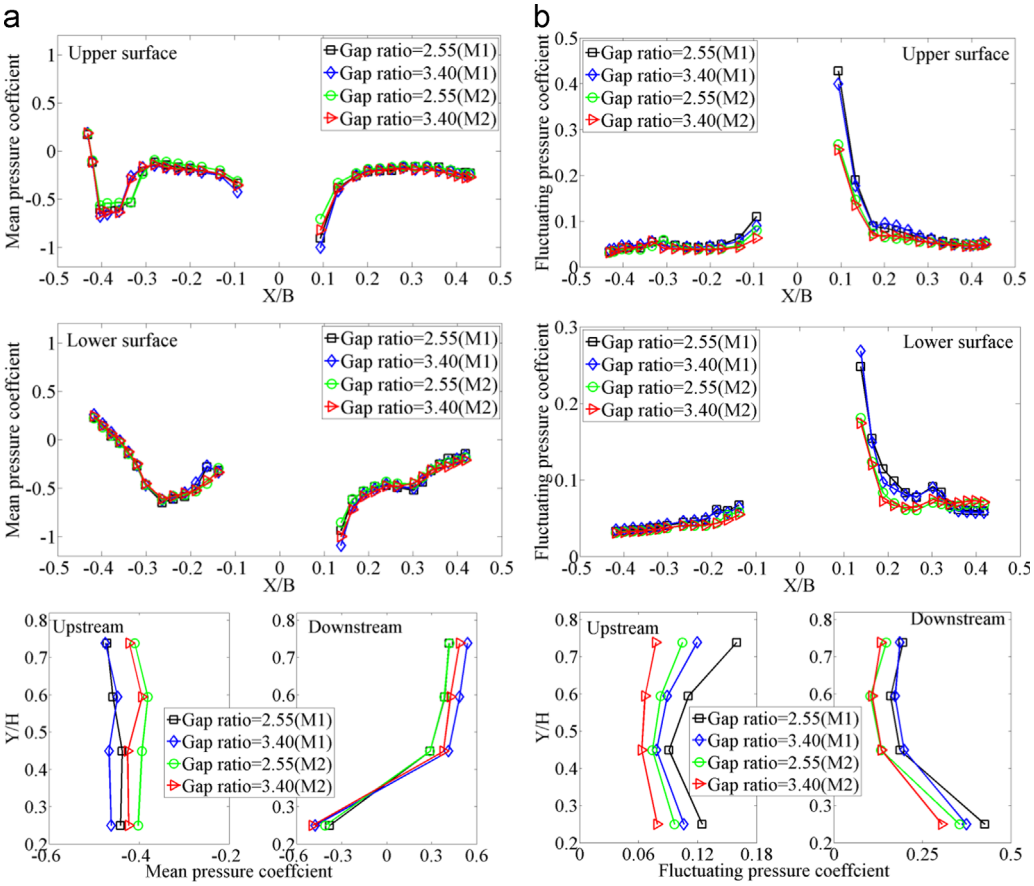

Fig. 15. Measured aerodynamic coefficients for the test models #1 and 2 with different gap ratios, (a) mean pressure coefficient and (b) fluctuating pressure coefficient.

where F_L, F_D and M are the lift force, the drag force, and the moment of the twin separated box girders, and C_L, C_D and C_M are the corresponding lift, drag, and moment coefficients. The pressures at the tip region of the windward girder have relatively higher amplitudes and will contribute considerably to the aerodynamic forces, particularly for the lift force; however, it is difficult to install the taps at the tip regions of the windward and leeward girders. Therefore, because of the present layout of the pressure taps neglects of the tip regions, some error is expected in the integral of the aerodynamic forces.

The mean and fluctuating values of the lift, drag, and moment force coefficients are calculated as shown in Fig. 12. For the wind condition employed in this study, i.e. zero degree angle of wind incidence, when the gap ratios change from smaller cases (i.e., gap ratio=0.85 and 1.70) to larger cases (i.e., gap ratio=2.55 and 3.40), the mean lift coefficient decreases; however, the drag and moment coefficients increase as shown in Fig. 12(a). The increase in the mean lift coefficient is mainly induced by the intense negative region of the mean pressure coefficients on the leeward girder at the larger gap ratios as shown in Fig. 11(a). The variation of mean pressure coefficient on both sides of the gap region (shown in Fig. 11(a)) causes the increase of the mean drag coefficients at the larger gap ratios. One reason for the increase in the mean moment coefficient is the increase in girder width with increasing gap ratios. For the wind condition employed in this study, i.e. zero degree angle of wind incidence, when the gap ratios change from smaller cases (i.e., gap ratio=0.85 and 1.70) to larger cases (i.e., gap ratio=2.55 and 3.40) the fluctuating lift, drag, and moment coefficients increase as shown in Fig. 12(b), which results from the increase in the fluctuating pressure coefficients on the leeward girder.

Using Eq. (6), the lift coefficient frequency spectra for the FBG models with different gap ratios are obtained as shown in Fig. 13. The larger gap ratio cases exhibit evident dominant frequencies of 96.67 and 104.7 Hz corresponding to the gap ratios of 2.55 and 3.40, respectively. The smaller gap ratio cases exhibit undistinguishable dominant frequencies of 11.42 and 15.22 Hz. The fluctuating parts of the pressure distributions in the frequency domain are calculated and the normalized amplitudes related to the vortex shedding frequencies are shown in Fig. 14. The results in Fig. 14 are similar with those in Fig. 11(b); thus, the fluctuating parts of the pressure distributions are mainly induced by the vortex shedding at larger gap ratio cases.

As mentioned above, there is no visible difference in the flow structures around two test models #1 and #2. A comparison of the distributions of the mean and fluctuating pressure coefficients was performed between the two test models at larger gap ratios (i.e., gap ratio=2.55 and 3.40) as shown in Fig. 15. As clearly shown in Fig. 15(a), the mean pressure coefficient distributions between these two models are very similar. The fluctuating pressure coefficient distribution are similar on the windward box except for a small variation on the trailing edge region; however, the fluctuating pressure coefficients on both sides of the gap region and the front parts of the leeward box of test model #1 are larger than the fluctuating pressure coefficients of test model #2. We hypothesize that the flow around test model #1 is more likely 2-D while the flow around test model #2 is more likely 3-D. Therefore, the vortex shedding is more intense for test model #1 and is weakened by the cross beams for test model #2.

4. Conclusion

In the present study, an experimental investigation was conducted to characterize the unsteady vortices and flow structures around fixed TBG bridge deck models with different gap ratios using PIV and pressure measurements. Important flow parameters, such as swirling strength, turbulent kinetic energy, and pressure fluctuations were employed to study the vortex shedding and flow structures around the fixed TBG models with different gap ratios.

The measurement results indicate clearly that the gap ratio brings a key influence on the flow structures around the TBG model. With gap ratio increasing from smaller cases (i.e., gap ratio=0.85 and 1.70) to larger cases (i.e., gap ratio=2.55 and 3.40), the vortices shed from the trailing edge of the windward box impinge on the leading edges of the leeward box and result in increased turbulent kinetic energy in the gap region and dramatically increased pressure fluctuations.

The gap width should be large enough (i.e., gap ratio=1.70) to keep the vortex shedding from the trailing edge of the windward box and make the vortex exist in the gap region. For the larger gap ratio cases (i.e., gap ratio=2.55 and 3.40), the dimensions of the vortices were not influenced by the gap width. However, for a small gap ratio case (i.e., gap ratio=1.70), the horizontal vortex dimension was compressed while the vertical vortex dimension was elongated, which limited the vortex shedding in the gap region. Therefore, the vortex shedding was predominately in the wake for the smaller gap ratio cases, while strong in both the wake and in the gap region for the larger gap ratio cases.

The results of the pressure field estimation and the measured pressure distribution verified that the pressure fluctuations on the leeward box of test model #1 increased with increasing gap ratio, while the pressure fluctuations on the leeward box were much larger than on the windward box at larger gap ratios (i.e., gap ratio=2.55 and 3.40).

Comparing with test model #1, cross beams could weaken the vortex shedding and decrease the pressure fluctuation on the leeward box to a certain extent for test model #2 with large gap ratios (i.e., gap ratio=2.55 and 3.40).

Acknowledgments

This research was funded by the National Natural Science Foundation of China (NSFC) (51378153, 51008093, 51161120359 and 91215302). The authors also want to thank Mr. Kai Zhang of Iowa State University for his help in manufacturing the test models.

References

Barlow, J.B., Rae, W.H., Pope, A., 1999. Low-speed Wind Tunnel Testing, 3rd ed. John Wiley & Sons, Inc., New York, pp. 330–375.

Diana, G., Resta, F., Zasso, A., Belloli, M., Rocchi, D., 2004. Forced motion and free motion aeroelastic tests on a new concept dynamometric section model of the Messina suspension bridge. J. Wind Eng. Ind. Aerodyn. 92, 441–462.

Diana, G., Resta, F., Belloli, M., Rocchi, D., 2006. On the vortex shedding forcing on suspension bridge deck. J. Wind Eng. Ind. Aerodyn. 94, 341–363.

Ge, Y.J., Xiang, H.F., 2008. Bluff body aerodynamics application in challenging bridge span length. In: Proceedings of 6th International Colloquium on Bluff Bodies Aerodynamics & Applications. July 20–24, Milano, Italy.

Irwin, H.P.A.H., Cooper, K.R., Girard, R., 1979. Correction of distortion effects caused by tubing systems in measurements of fluctuating pressures. J. Wind Eng. Ind. Aerodyn. 5, 93–107.

Kwok, K.C.S., Qin, X.R., Fok, C.H., Hitchcock, P.A., 2012. Wind-induced pressures around a sectional twin-deck bridge model: effects of gap-width on the aerodynamic forces and vortex shedding mechanisms. J. Wind Eng. Ind. Aerodyn. 110, 50–61.

Laima, S.J., Li, H., Chen, W.L., Li, F.C., 2013. Investigation and control of vortex-induced vibration of twin box girders. J. Fluids Struct. 39, 205–221.

Larsen, A., Savage, M., Lafrenière, A., Hui, M.C.H., Lansen, S.V., 2008. Investigation of vortex response of a twin box bridge section at high and low Reynolds numbers. J. Wind Eng. Ind. Aerodyn. 96, 934–944.

Ogawa, K., Shimodoi, H., Oryu, T., 2002. Aerodynamic characteristics of a 2-box girder section adaptable for a super-long span suspension bridge. J. Wind Eng. Ind. Aerodyn. 90, 2033–2043.